nature portfolio

https://doi.org/10.1038/s41563-021-01141-w

Supplementary information

Direct visualization of the three-dimensional shape of skyrmion strings in a noncentrosymmetric magnet

In the format provided by the authors and unedited

Supplementary information: Direct visualization of the three-dimensional shape of skyrmion strings in a noncentrosymmetric magnet

S. Seki[1,2,3,4,*], M. Suzuki[5,6*], M. Ishibashi[7], R. Takagi[1,2,3], N. D. Khanh[3],
Y. Shiota[7], K. Shibata[8], W. Koshibae[3], Y. Tokura[1,3,9], T. Ono[7,10,*]

[1] *Department of Applied Physics, University of Tokyo, Tokyo 113-8656, Japan,*
[2] *Institute of Engineering Innovation,*
University of Tokyo, Tokyo 113-8656, Japan,
[3] *RIKEN Center for Emergent Matter Science (CEMS), Wako 351-0198, Japan,*
[4] *PRESTO, Japan Science and Technology Agency (JST), Kawaguchi 332-0012, Japan,*
[5] *Japan Synchrotron Radiation Research Institute, Sayo 679-5198, Japan,*
[6] *School of Engineering, Kwansei Gakuin University, Sanda 669-1337, Japan,*
[7] *Institute for Chemical Research, Kyoto University, Uji 611-0011, Japan,*
[8] *Institute of Industrial Science, The University of Tokyo, 153-8505 Tokyo, Japan,*
[9] *Tokyo College, University of Tokyo, Tokyo 113-8656, Japan,*
[10] *Center for Spintronics Research Network,*
Graduate School of Engineering Science,
Osaka University, Toyonaka 560-853, Japan

I. ENERGY DEPENDENCE OF X-RAY ABSORPTION AND MAGNETIC CIRCULAR DICHROISM

In the present study, the absorption coefficient ($\mu = -\ln(I_t/I_0)$ with I_t and I_0 being the intensity of the transmitted and incident X-ray beam, respectively) for the left- and right-handed circular polarized beam (μ^+ and μ^-, respectively) was measured for $Mn_{1.4}Pt_{0.9}Pd_{0.1}Sn$ with the experimental setup as shown in Fig. 1c in the main text. Supplementary Figs. 1a and b indicate the spectra of X-ray magnetic circular dichroism (XMCD) $\Delta\mu = (\mu^+ - \mu^-)$ and polarization-averaged X-ray absorption $\bar{\mu} = (\mu^+ + \mu^-)/2$ measured at +999 mT and -996 mT (i.e. the positively and negatively saturated uniform magnetic state, respectively). To obtain the largest amplitude of XMCD contrast, the X-ray energy was tuned at 11.572 keV in resonance with the L_3 absorption edge of Pt in the scalar magnetic tomography measurements. Note that the magnetism in this compound is mainly governed by Mn sites, while the electrons of Pt sites are also magnetically polarized through the hybridization between Pt 5d orbitals and Mn 3d orbitals.

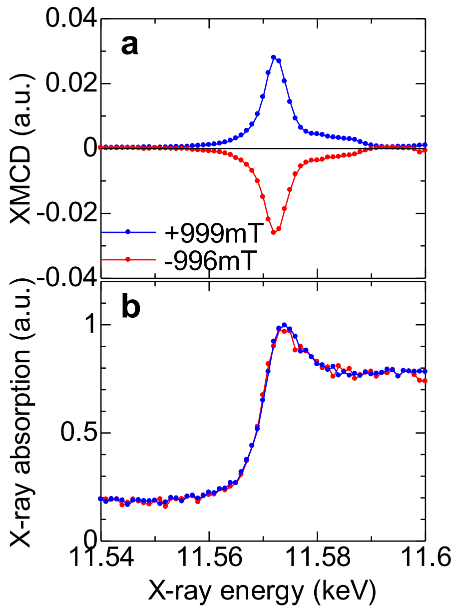

Supplementary Fig. 1: **XMCD and X-ray absorption spectra**. **a,b** Spectra of X-ray magnetic circular dichroism (XMCD) $\Delta\mu$ (**a**) and X-ray absorption $\bar{\mu}$ (**b**) measured for $Mn_{1.4}Pt_{0.9}Pd_{0.1}Sn$. The directions of incident X-ray beam and external magnetic field are parallel to the [001] axis. The blue and red data points are measured with +999 mT and -996 mT.

II. DETAILED EXPERIMENTAL CONFIGURATION FOR SCALAR MAGNETIC X-RAY TOMOGRAPHY MEASUREMENTS

Supplementary Fig. 2 shows the detailed experimental setup for scalar magnetic X-ray tomography measurements. The wedge-shaped $Mn_{1.4}Pt_{0.9}Pd_{0.1}Sn$ sample was placed on the top of a projection-type electromagnet, and both were mounted on the same rotation stage (θ) and two-dimensional translation (X-Z) stages. In this system, the sample and the electromagnet were rotated and moved while the relative orientation of the sample crystal axis and the magnetic field was unchanged during tomographic data acquisition. The magnetic field was generated by the coils inside the magnet body and drawn through the outer pole to the sample position, magnetizing the sample in the horizontal direction. Since the sample and the X-ray beam were at a height of about 1 mm above the surface of the pole, the incident and transmitted X-ray beams were unobstructed in any of the 360° directions. This setup made it possible to perform X-ray tomography measurements under magnetic fields.

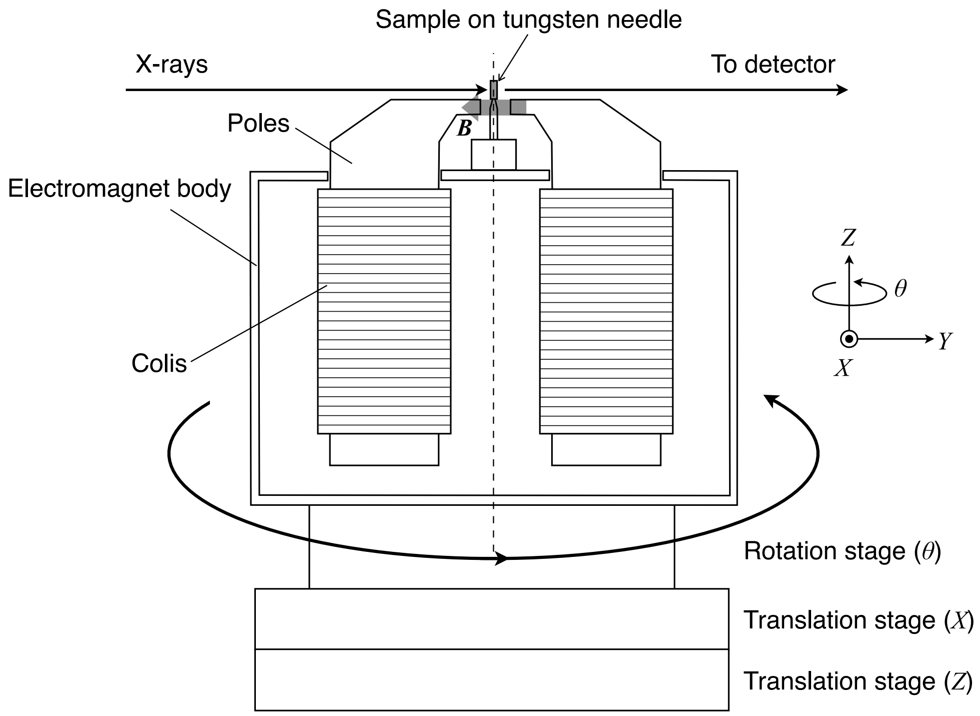

Supplementary Fig. 2: **An experimental setup of the scanning hard-X-ray microtomography measurement under external magnetic fields**.

III. COMPARISON OF MEASURED AND REPRODUCED XMCD IMAGES

To confirm the reliability of the 3D tomographic imaging approach, the measured (Supplementary Figs. 3a-e) and reproduced (Supplementary Figs. 3f-j) XMCD images for selected θ values are compared in Supplementary Fig. 3. Here, the latter images are simulated based on the tomographically reconstructed $m^c(\mathbf{r})$ profiles and Eq. (1) in the main text. We can see that the measured and reproduced data agree well with each other for all θ values, demonstrating the validity of the present tomographic reconstruction process.

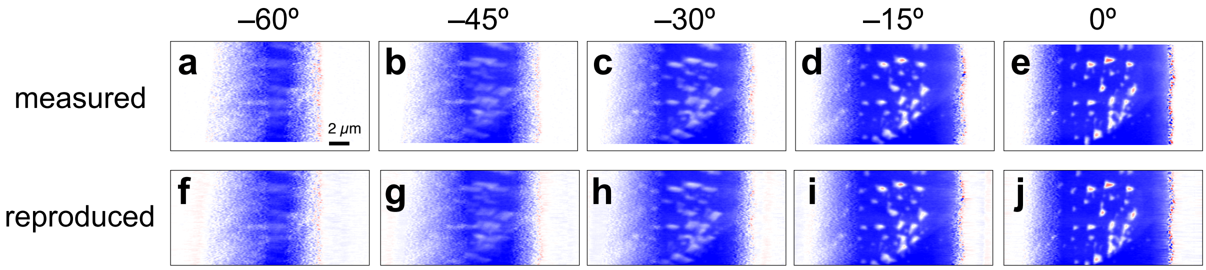

Supplementary Fig. 3: **Comparison of measured and reproduced XMCD projection images.** **a-e**, XMCD images experimentally measured at $B = 437$ mT at different projection angles θ, which are the same as the ones presented in Fig. 2 in the main text. **f-j**, The corresponding XMCD images simulated based on Eq. (1) in the main text and the tomographically reconstructed $m^c(\mathbf{r})$ profile.

IV. MICROMAGNETIC SIMULATION OF SPATIAL DISTRIBUTION OF LOCAL MAGNETIZATION AND EMERGENT MAGNETIC FIELD

To estimate the 3D spatial distribution of vector magnetization $\mathbf{m}(\mathbf{r}) \equiv \mathbf{m}_\mathbf{r}$ in the system with the D_{2d} crystal lattice symmetry, we performed the micromagnetic simulation based on Landau-Lifshitz-Gilbert (LLG) equation with the magnetic Hamiltonian described as

$$\begin{aligned}\mathcal{H} = &- J\sum_{\mathbf{r}} \mathbf{m}_\mathbf{r} \cdot (\mathbf{m}_{\mathbf{r}+\hat{\mathbf{a}}} + \mathbf{m}_{\mathbf{r}+\hat{\mathbf{b}}} + \mathbf{m}_{\mathbf{r}+\hat{\mathbf{c}}}) + D\sum_{\mathbf{r}}[\hat{\mathbf{a}} \cdot (\mathbf{m}_\mathbf{r} \times \mathbf{m}_{\mathbf{r}+\hat{\mathbf{a}}}) - \hat{\mathbf{b}} \cdot (\mathbf{m}_\mathbf{r} \times \mathbf{m}_{\mathbf{r}+\hat{\mathbf{b}}})] \\ &- K_{\text{imp}} \sum_{\mathbf{r}\in\Lambda} (m^c_\mathbf{r})^2 - B\sum_{\mathbf{r}} m^c_\mathbf{r}.\end{aligned} \tag{S1}$$

$\hat{\mathbf{a}}$, $\hat{\mathbf{b}}$ and $\hat{\mathbf{c}}$ are the unit vectors along the [100], [010] and [001] directions, and $m^c_{\mathbf{r}}$ is the [001] component of $\mathbf{m}_{\mathbf{r}}$. J, D, and B represent the amplitude of exchange interaction, Dzyaloshinskii-Moriya (DM) interaction, and external magnetic field along the [001] direction, respectively. The single-ion magnetic anisotropy K_{imp} is introduced on the random sites $\mathbf{r} \in \Lambda$, which effectively represents the crystallographic defects[S2] (i.e. Mn-site vacancy and Pt/Pd anti-site disorder reported in Ref. [S1] as well as the defects introduced through the FIB fabrication process) expected in the present $Mn_{1.4}Pt_{0.9}Pd_{0.1}Sn$ crystals. It contributes to keep the metastable states (such as Y-shaped or interrupted skyrmion string structures) from relaxing into more stable states, leading to the long lifetime of distorted

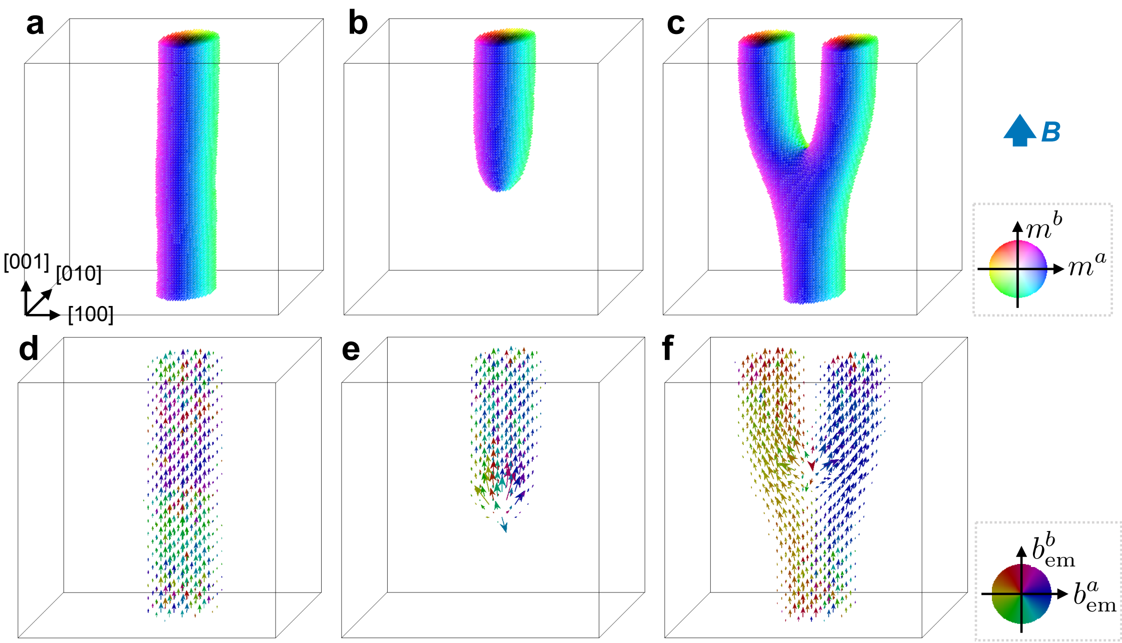

Supplementary Fig. 4: **Simulated spatial distribution of local magnetization and emergent magnetic field**. **a-c**, Simulated spatial distribution of local magnetic moment $\mathbf{m}$ for the genuine (**a**), interrupted (**b**), and Y-shaped (**c**) skyrmion strings. Here, the hue and brightness of background color represent the in-plane and out-of-plane component of $\mathbf{m}$, respectively, and the length of magnetic moment is fixed to $|\mathbf{m}(\mathbf{r})| = 1$. Note that we do not put color for $m^c > 0.5.$, i.e. the outside of the skyrmion string, to make the three-dimensional magnetic texture clear. **d-f**, The corresponding spatial distribution of emergent magnetic field $\mathbf{b}_{\mathrm{em}}$. The color of the arrows reflect the in-plane component of $\mathbf{b}_{\mathrm{em}}$. See the text for the detailed parameters used in the simulation.

or interrupted skyrmion string structure. The length of local magnetic moment is fixed to $|\mathbf{m_r}| = 1$, and the detailed parameter sets in the present simulation is provided in Methods section in the main text.

Supplementary Fig. 4a indicates the typical magnetic moment distribution $\mathbf{m}(\mathbf{r})$ for a genuine skyrmion string obtained in the simulation. Here, skyrmion string core is characterized by the magnetic moment antiparallel to B, which is embedded in the ferromagnetic background with moment parallel to B. At the intermediate region, the in-plane component of magnetic moment (m^a and m^b) shows anti-vortex-type arrangement, reflecting the D_{2d} symmetry of DM interaction. The spin swirling manner obtained in this simulation is the same as the one experimentally observed in Ref. [S1], which is often called anti-skyrmion. In the similar manner, the interrupted (Supplementary Fig. 4b) and Y-shaped (Supplementary Fig. 4c) skyrmion string can be also obtained in the simulation as the metastable states.

In general, the conduction electrons interacting with such spin textures feel the the emergent magnetic field $\mathbf{b}_{\text{em}}(\mathbf{r})$ associated with quantum Berry phase[S3], which is given by

$$b_{\text{em}}^{\alpha}(\mathbf{r}) = (\epsilon^{\alpha\beta\gamma}/4)\mathbf{n_r} \cdot (\partial_\beta \mathbf{n_r} \times \partial_\gamma \mathbf{n_r}). \tag{S2}$$

$\epsilon^{\alpha\beta\gamma}$ is the totally antisymmetric tensor in the three dimensions. In Supplementary Figs. 4d-f, the spatial distribution of $\mathbf{b}_{\text{em}}(\mathbf{r})$ for each spin texture is indicated. In case of the genuine skyrmion string (Supplementary Figs. 4a and d), the local emergent magnetic field is aligned along the direction of string. On the other hand, the interrupted (Supplementary Figs. 4b and e) and Y-shaped (Supplementary Figs. 4c and f) skyrmion strings are characterized by the divergence of emergent magnetic field $\nabla \cdot \mathbf{b}_{\text{em}} \neq 0$ at the termination or merging point of string, which can be considered as the monopole of emergent magnetic flux (i.e. emergent magnetic monopole). The appearance of similar emergent magnetic monopole has also been predicted theoretically for Bloch-type skyrmions in the chiral lattice system[S4, S5].

V. MICROMAGNETIC SIMULATION WITH DEMAGNETIZATION FIELDS

According to the recent MFM experiments[S6], the skyrmion diameter λ_{sk} in $Mn_{1.4}Pt_{0.9}Pd_{0.1}Sn$ linearly increases as a function of the sample thickness t, and $\lambda_{\text{sk}} \sim 1$ μm for $t \sim 4$ μm has been reported in consistent with our present observation. The associated theoretical analysis in Ref. [S6] suggests that the skyrmion diameter in this compound

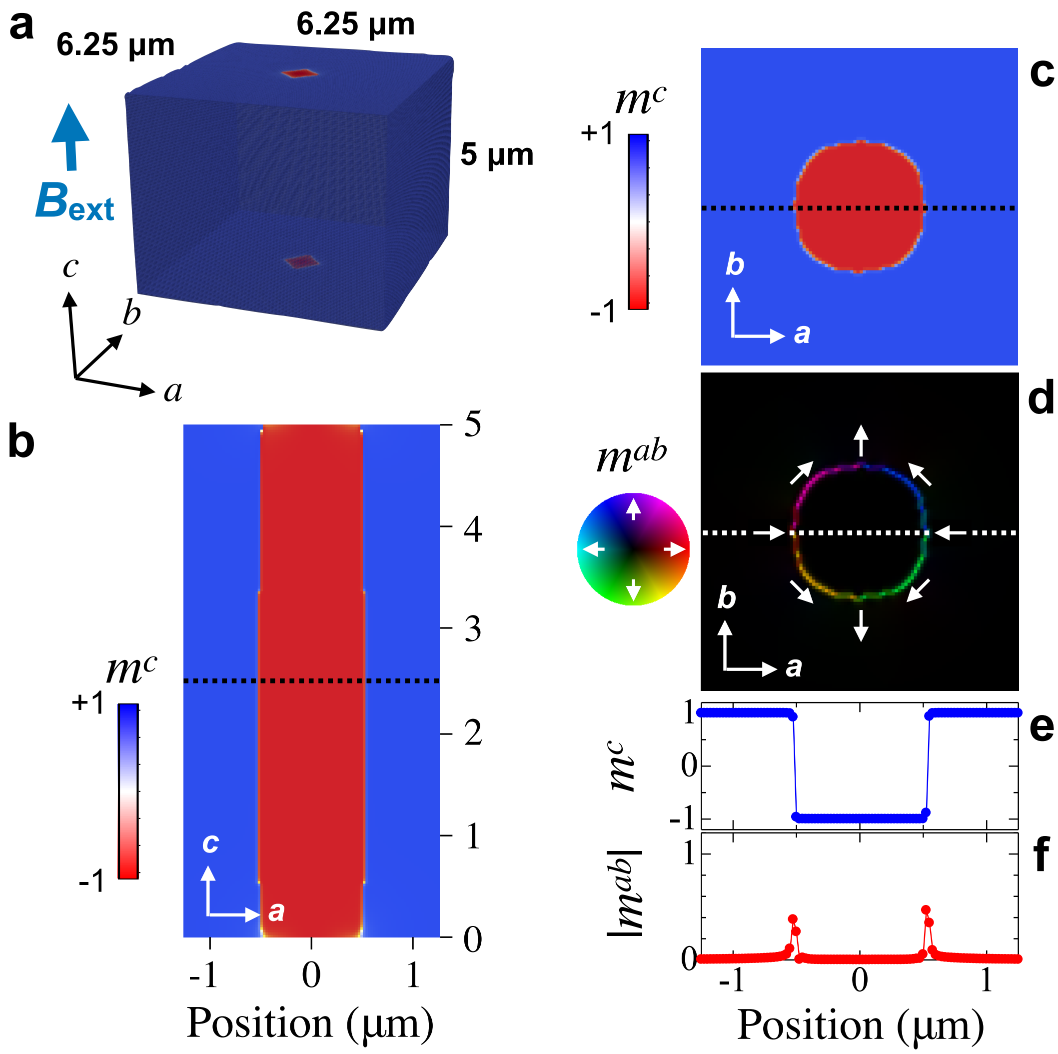

Supplementary Fig. 5: **Micromagnetic simulation considering demagnetization fields**. **a**, Schematic illustration of system dimensions employed for micromagnetic simulation. The simulation was performed with external magnetic field $\mathbf{B}_{\text{ext}} = 400$ mT. **b**, *ac*-plane cross section of the simulation results, which cuts a straight skyrmion string running along the $\mathbf{B}_{\text{ext}} \parallel [001]$ direction. The background color represents the *c*-component of local magnetization $\mathbf{m}$ (m^c). **c**,**d** *ab*-plane cross section of the simulation results, which corresponds to the dashed line in **b**. The background color represents the m^c and m^{ab} (i.e. m^a and m^b) components, respectively. For the latter case, the hue and brightness represent the orientation and amplitude of m^{ab} component, respectively, as indicated by the color wheel. For clarity, the corresponding spin orientation is also presented by white arrows. **e**,**f**, Line profile of m^c and $|m^{ab}|(= |m^a + im^b|)$, obtained for the dashed lines in **c** and **d**.

is affected not only by exchange and DM interaction, but also by magnetic dipole-dipole interaction (i.e. demagnetization field) and uniaxial anisotropy.

To understand the stable spin texture in the $Mn_{1.4}Pt_{0.9}Pd_{0.1}Sn$ sample with the thickness in order of 5 μm (as employed in our experiments in the main text), we have performed additional micromagnetic simulation considering demagnetization fields and uniaxial anisotropy based on LLG equation by using MuMax3 software, which was modified to include an anisotropic DM interaction[S7]. The stable magnetization distribution $\mathbf{m}(\mathbf{r})$ was deduced by minimizing the magnetic free energy $E = \int \epsilon(\mathbf{r}) d\mathbf{r}$ with energy density given by

$$\begin{aligned} \epsilon =& A[(\partial_a \mathbf{m})^2 + (\partial_b \mathbf{m})^2 + (\partial_c \mathbf{m})^2] + D[m^c \frac{\partial m^a}{\partial a} - m^a \frac{\partial m^c}{\partial a} - m^c \frac{\partial m^b}{\partial b} + m^b \frac{\partial m^c}{\partial b}] \\ & - K_{\mathrm{u}} (m^c)^2 + M_s \mathbf{B}_{\mathrm{ext}} \cdot \mathbf{m} - \frac{1}{2} M_s \mathbf{B}_{\mathrm{d}} \cdot \mathbf{m}, \end{aligned} \quad \text{(S3)}$$

where $\mathbf{B}_{\mathrm{ext}}$ and $\mathbf{B}_{\mathrm{d}}$ represent the external magnetic field and demagnetization field, respectively. We tentatively employed the exchange stiffness constant $A = 3 \times 10^{-11}$ J m^{-1}, anisotropic DM interaction constant $D = 2 \times 10^{-3}$ J m^{-2}, uniaxial anisotropy constant $K_{\mathrm{u}} = 2 \times 10^5$ J m^{-3}, and saturated magnetization $M_s = 445 \times 10^3$ A m^{-1}, which are close to the parameters previously proposed for $Mn_{1.4}Pt_{0.9}Pd_{0.1}Sn$[S1, S6, S8]. The simulation was performed for the system size of $6.25 \times 6.25 \times 5 \mu\mathrm{m}^3$ with mesh sizes of $25 \times 25 \times 25$ nm^3 under periodic boundary conditions along the a and b directions and Gilbert damping constant $\alpha = 0.3$.

Supplementary Fig. 5 summarizes the result of micromagnetic simulation for isolated skyrmion string, obtained with $|\mathbf{B}_{\mathrm{ext}}| = 400$ mT applied along the c-direction. The spatial distribution of m^c for the ac-plane cross section is shown in Supplementary Fig. 5b, where the skyrmion string with the core diameter ~ 1 μm runs along the c-axis. Supplementary Figs. 5c and d indicate the ab-plane cross section showing the spatial distribution of out-of-plane (m^c) and in-plane (m^a and m^b) magnetization components, respectively. The in-plane magnetization component shows anti-vortex-like arrangement, in consistent with the D_{2d} symmetry of DM interaction. The corresponding line profiles along the dashed line in each figure are indicated in Supplementary Figs. 5e and f, which suggests that the thickness of the wall region with in-plane magnetization component $|m^{ab}| = |m^a + im^b|$ is less than 100 nm.

The above results confirm that the skyrmion string structure with up to 1 μm core diameter can be stabilized for the 5 μm-thick sample, in consistent with our experimental observations. The expected thickness of the wall region with in-plane magnetization component (< 100 nm) is much smaller than the skyrmion core diameter ($\sim 1\mu$m), which supports the validity of our tomographic reconstruction approach focusing on the m^c component. The present simulation also confirms that the swirling manner of in-plane magnetization component is still governed by DM interaction, suggesting that the overall feature of $\mathbf{b}_{\rm em}$ distribution shown in Supplementary Fig. 4 remains unchanged even with demagnetization fields. In the process of the relaxation into the stable state as shown in Supplementary Fig. 5, the skyrmion string structure with slightly distorted (i.e. not circular) core shape temporarily appears, whose arrangement of in-plane magnetization component is also confirmed to be anti-vortex-type in consistent with the D_{2d} symmetry of DM interaction.

VI. THICKNESS GRADIENT OF THE SAMPLE

To clarify the position dependence of the sample thickness, the line profiles of X-ray absorption intensity are summarized in Supplementary Fig. 6. They indicate that the

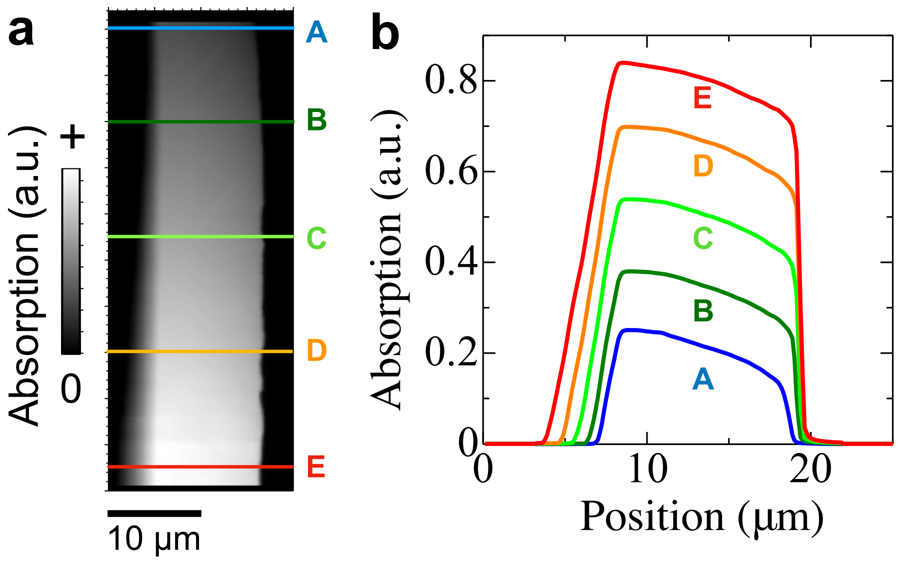

Supplementary Fig. 6: **Line profiles of sample thickness**. **a**, X-ray absorption (XAS) image of the plate-shaped $Mn_{1.4}Pt_{0.9}Pd_{0.1}Sn$ sample viewed from the out-of-plane [001] direction, which is the same as Fig. 1g in the main text. **b**, Line profiles of X-ray absorption intensity along the lines A-E in **a**, which corresponds to the position dependence of the sample thickness.

present plate-shaped $Mn_{1.4}Pt_{0.9}Pd_{0.1}Sn$ sample has the thickness gradient not only along the long axis but also along the short axis. The sample becomes thinner in the upper right region, in which the magnetic contrast is blurred as confirmed in the XMCD images in Figs. 2a-g in the main text. The observed loss of XMCD contrast is probably because the magnetic modulation period $\lambda_{\rm mag}$ in the thinner part ($\lambda_{\rm mag} \sim 130$ nm according to Refs. [S1, S6]) is smaller than the spatial resolution of the XMCD measurements. In addition, the focused ion beam (FIB) micro-fabrication process always makes some damaged layer at the sample surface, which also causes the loss of magnetic contrast in the thinner part.

VII. VALIDITY OF TOMOGRAPHIC RECONSTRUCTION PROCEDURE FOCUSING ON m^c

In this section, we discuss the validity of our tomographic reconstruction procedure employed in the main text. In the present experiments, the XMCD image is taken in the X-Y-Z coordinates fixed to the measurement system (Supplementary Fig. 7a and Figs. 1c and d in the main text). The direction of incident X-ray beam is defined as the Y-axis, and θ represents the angle between the Y-axis and the [001] axis of the sample. The rotation axis of the sample is defined as the Z-axis, which is set parallel to the [100] crystallographic axis. Here, we define the magnetization distribution in the coordinates $\mathbf{r} = Z\mathbf{a} + x\mathbf{b} + y\mathbf{c}$ fixed to the crystallographic axes of the sample. For the specific value of Z and θ, the relation between the magnetization distribution $\mathbf{m}(x, y)$ and the XMCD contrast $\Delta\mu(X, \theta)$ is given by

$$\Delta\mu(X, \theta) = \int [m^a(x, y) \sin\theta + m^c(x, y) \cos\theta] dY. \tag{S4}$$

According to the recent single crystal magnetization measurements[S1, S9, S10], our target compound is characterized by easy-axis magnetic anisotropy, where magnetic moment favors to be aligned parallel to the [001] axis. This is consistent with the experimentally observed XMCD contrast for $\theta = 0$ (Figs. 2a-g in the main text), where the peripheral and core region of circular or stripe-like pattern are characterized by the almost saturated amplitude of $+m^c$ and $-m^c$, respectively. On the basis of the above knowledge, we assumed that the m_c component is dominant, and performed the tomographic reconstruction based on the approximate expression

$$\Delta\mu(X,\theta) \approx \int [m^c(x,y)\cos\theta] dY, \tag{S5}$$

which is identical with Eq. (1) in the main text.

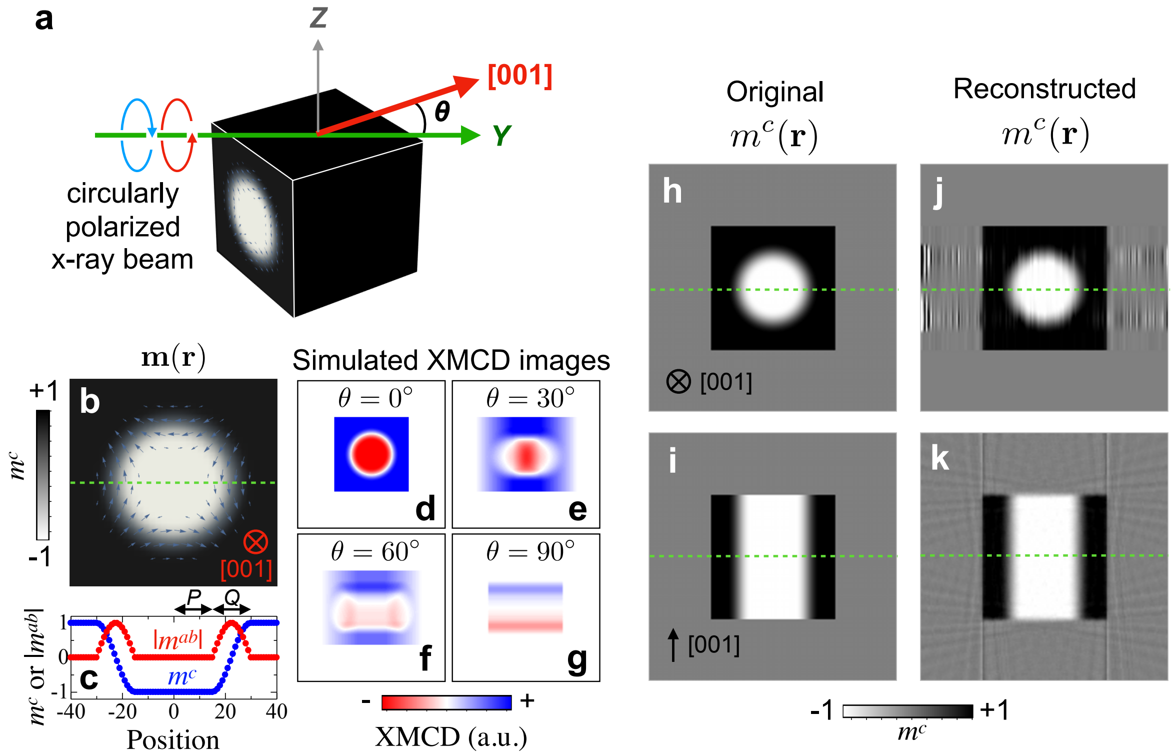

Supplementary Fig. 7: **Simulation of tomographic reconstruction process for an isolated skyrmion string**. **a**, Schematic illustration of the configuration used for the simulation, which mimics the one shown in Fig. 1c in the main text. **b**, Magnetization distribution defined by Eq. S6, viewed from the [001] direction. The arrows and background color represent the in-plane (m^a and m^b) and out-of-plane (m^c) component of **m**, respectively. **c**, The corresponding line profile of m^c (blue) and $|m^{ab}| = |m^a + im^b|$ (red) along the dashed line in **b**. **d-g**, The simulated XMCD images, calculated based on Eq. S4 with the various view angle θ for the spin texture in **b**. The color scale represents the XMCD contrast $\Delta\mu$. **h**,**i**, The spatial distribution of m^c for the original model defined by Eq. S6 (**b**), viewed from the direction parallel (**h**) and perpendicular (**i**) to the [001] axis, respectively. Here, each cross section corresponds to the dashed line in the other image. **j**,**k** The m^c distribution reconstructed based on Eq. S5, from a series of simulated XMCD images as shown in **d-g**. This reconstruction process is the same as the one employed in the main text.

In the following, we discuss how this approximation affects the reconstruction process. As a simple example, we assumed a straight skyrmion string with anti-vortex-type arrangement of in-plane magnetization component embedded in the ferromagnetic background as shown in Supplementary Fig. 7b, whose magnetization distribution $\mathbf{m}(\mathbf{r})$ is described by

$$(m^a, m^b, m^c) = \begin{cases} (0, 0, -1) & (r_{\rm in} < P) \\ (\sin\phi\sin\psi, \cos\phi\sin\psi, -\cos\psi) & (P \leq r_{\rm in} \leq P + Q) \\ (0, 0, 1) & (P + Q < r_{\rm in}) \end{cases} \tag{S6}$$

Here, we defined $\mathbf{r} = Z\mathbf{a} + x\mathbf{b} + y\mathbf{c} = [r_{\rm in}\cos\phi]\mathbf{a} + [r_{\rm in}\sin\phi]\mathbf{b} + y\mathbf{c}$ and $\psi = \pi(P - r_{\rm in})/Q$. In this model, the uniform $-m^c$ component is dominant for the cylindrical region with $r_{\rm in} < P$, and in-plane magnetization component (i.e. m^a and m^b) appears only for the intermediate region with the thickness of Q. For $P + Q < r_{\rm in}$, the uniform $+m^c$ component is dominant (Supplementary Fig. 7c). In the present model, we assumed the cubic-shaped sample with the dimension $80 \times 80 \times 80$, where a single skyrmion string with $P = 15$ and $Q = 15$ is embedded.

First, we have numerically simulated its XMCD patterns for various view angles θ ($-90^\circ \leq \theta \leq 90^\circ$ with 5° steps) based on Eqs. S4 and S6 as shown in Supplementary Figs. 7d-g. Next, based on these simulated XMCD images, we have performed the tomographic reconstruction of $m^c(\mathbf{r})$ using Eq. S5. In Supplementary Figs. 7h-k, the original and reconstructed $m^c(\mathbf{r})$ profiles are compared. The overall three-dimensional shape of skyrmion string is well reproduced, which confirms the validity of our tomographic reconstruction approach based on Eq. S5 (i.e. the one employed in the main text). Note that the reconstructed $m^c(\mathbf{r})$ profile contains small amount of artifacts, which reflects the ignorance of m^a component in the reconstruction process. Considering the result of micromagnetic simulation in Supplementary Note V and Supplementary Fig. 5, the Q/P ratio (i.e. the relative thickness of the wall region with in-plane magnetization component) in our $Mn_{1.4}Pt_{0.9}Pd_{0.1}Sn$ sample is probably smaller than the above model, suggesting that the artifacts in the actual experiments would be more suppressed. Since the spot size of X-ray beam in our experiment is 150×150 nm^2 in full width at half maximum (FWHM), the spatial resolution of the present scalar magnetic tomography would be in order of a few hundred nanometers.

VIII. ANALYSIS OF NOISE IN THE RECONSTRUCTED $m^c(\mathbf{r})$ PROFILE

In the following, we discuss the noise in the reconstructed $m^c(\mathbf{r})$ profiles. As discussed in Supplementary Note VII and Supplementary Fig. 7, the present tomographic reconstruction process ignores the $m^a(\mathbf{r})$ component and often leads to some minor artifacts. Additionally, scratch-like noise can be seen in Supplementary Fig. 7k, which is mainly due to the limited number of projection angles θ.

To evaluate the possible noise contribution, we have applied binomial smoothing[S11] to the original $m^c(\mathbf{r})$ profile to suppress the high-frequency components. Here, a bionominal filter with a $5 \times 5 \times 5$ kernel ($n = 2$) was adopted for the reconstructed data with a voxel size of $50 \times 50 \times 50$ nm^3, giving a cut-off frequency of $q_c = 3.64\mu\text{m}^{-1}$ in the [100], [010], and [001] directions. The corresponding spatial resolution of the filtered image was $1/2q_c = 137$

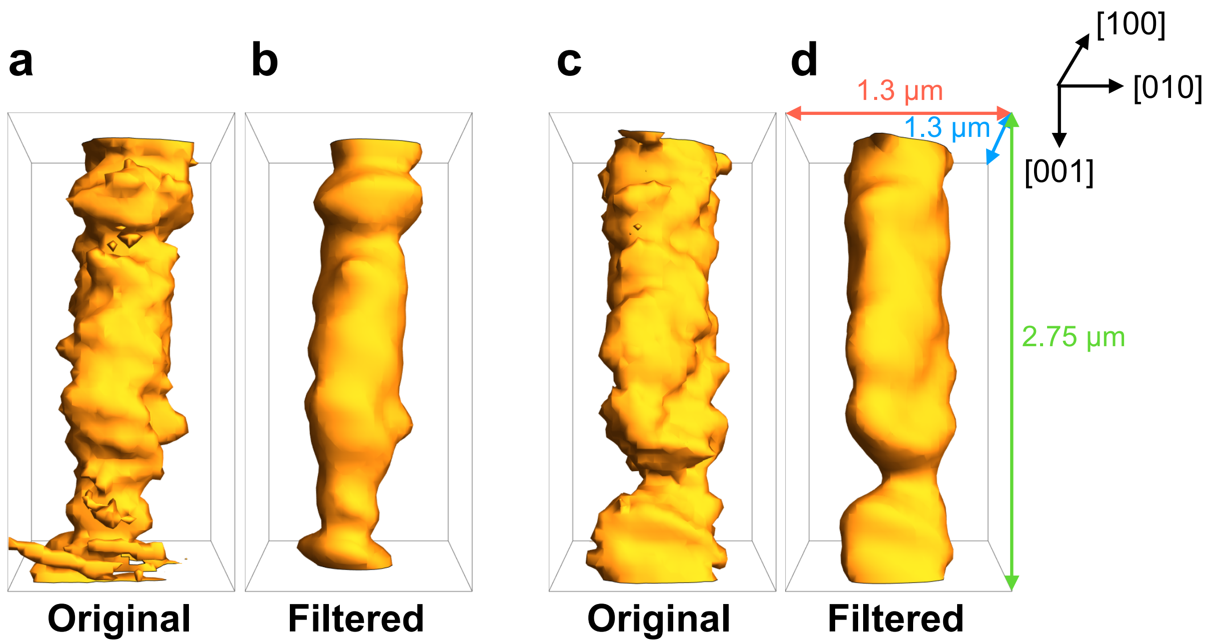

Supplementary Fig. 8: **Skyrmion string shapes obtained from the original and filtered $m^c(\mathbf{r})$ profiles.** **a**,**c**, The 3D shape of skyrmion strings obtained from the original $m^c(\mathbf{r})$ profile at 437 mT. **b**,**d**, The corresponding images obtained from the filtered $m^c(\mathbf{r})$ profile, where the higher frequency component (with the period shorter than the X-ray beam spot size ~ 150 nm) is removed to suppress the possible noise contribution. These filtered images are shown as Figs. 4e and h in the main text.

nm, i.e. almost equivalent to the X-ray beam spot size (~ 150 nm).

In Supplementary Fig. 8, skyrmion string shapes obtained from the original and filtered $m^c(\mathbf{r})$ profiles are compared. While the filtered one is characterized by a smoother surface, there remains a considerable depth dependence of the cross-sectional outline of skyrmion strings. Therefore, we expect that the observed deformation of the skyrmion string shape is probably intrinsic and reflects the frequent pinning of the skyrmion wall region by crystallographic defects.

In the present study, we employed the standard algorithm of the algebraic reconstruction technique (ART)[S12] to obtain the $m^c(\mathbf{r})$ profile from the experimental data. Alternatively, it might be possible to obtain highly accurate reconstructed images from a small number of projections using the compressed-sensing algorithms recently proposed[S13]. To the best of our knowledge, the compressed-sensing algorithm has not been applied to X-ray magnetic tomography. The further improvement of the tomographic reconstruction algorithm and the better analysis of the depth profile of skyrmion string shapes are the issue for future study.

IX. POSSIBLE TEXTURES OF THE IN-PLANE MAGNETIZATION COMPONENT

For $Mn_{1.4}Pt_{0.9}Pd_{0.1}Sn$ with D_{2d} crystal lattice symmetry, the appearance of anti-skyrmion spin texture (i.e. skyrmion with anti-vortex-like arrangement of in-plane magnetization component) has been reported for $B \parallel [001]$, and we expect that the similar spin swirling manner is realized in our present sample. This is also supported by the micromagnetic simulation results in Supplementary Fig. 5, where the arrangement of in-plane magnetization component is confirmed to be governed by DM interaction even under the existence of demagnetization fields.

Note that the recent Lorentz transmission electron microscopy experiments suggest that the tilting of the magnetic field from the [001] axis often induces the transition from the anti-skyrmion to Bloch skyrmion (characterized by the vortex-like arrangement of in-plane magnetization component)[S8, S14]. This phenomena is related with the induction of the chirality by the in-plane B component, which is commonly observed in the crystal system with D_{2d} symmetry[S15]. In case of such Bloch skyrmions induced by tilted magnetic field, the m^c distribution turns into elliptical and their long-axis is aligned along the $\langle 100 \rangle$

direction[S8, S14].

In our present XMCD images (Figs. 4a-d in the main text), the observed shape of skyrmion core is not always circular, while their distortion manner seems rather random. As discussed in the main text, the crystal structure of $Mn_{1.4}Pt_{0.9}Pd_{0.1}Sn$ contains many vacancy and randomly occupied sites[S1], and the FIB micro-fabrication process using Ga-ion irradiation also causes some unintentional defects. Therefore, we expect that the observed distortion of skyrmion core shape is mainly governed by the random pinning of skyrmion wall region, rather than the tilting of magnetic field from the [001] axis.

According to the micromagnetic simulation results in Supplementary Fig. 5, the expected thickness of the wall region with in-plane magnetization component (< 100 nm) is smaller than the spatial resolution of our present experimental setup ($\sim$ a few hundred nanometers). Therefore, the reliable reconstruction of the in-plane magnetization component is not possible at this stage. To experimentally reconstruct the all three magnetization components (i.e. vector magnetic tomography), the further development of two-axes rotation system with tunable magnetic field source as well as better spatial resolution would be required, which is the issue for the future study. In principle, our present scalar magnetic X-ray tomography technique with tunable magnetic field can visualize the three-dimensional shape of any types of skyrmion string structures, which will contribute to the further investigation of the creation, annihilation and transfer process of these topological objects.

[S1] A. K. Nayak *et al.*, Magnetic antiskyrmions above room temperature in tetragonal Heusler materials. Nature **548**, 561 (2017).

[S2] W. Koshibae and N. Nagaosa, Dynamics of skyrmion in disordered chiral magnet of thin film form. Sci. Rep. **9**, 5111 (2019).

[S3] N. Nagaosa, Y. Tokura, Topological properties and dynamics of magnetic skyrmions. Nature Nanotech. **8**, 899 (2013).

[S4] P. Milde *et al.*, Unwinding of a Skyrmion Lattice by Magnetic Monopoles. Science **340**, 1076 (2013).

[S5] F. N. Rybakov *et al.*, New Type of Stable Particlelike States in Chiral Magnets. Phys. Rev. Lett. **115**, 117201 (2015).

[S6] T. Ma *et al.*, Tunable Magnetic Antiskyrmion Size and Helical Period from Nanometers to Micrometers in a D_{2d} Heusler Compound. Adv. Mater. **32** 2002043 (2020).

[S7] A. Vansteenkiste *et al.*, The design and verification of MuMax3. AIP Advances **4**, 107133 (2014).

[S8] J. Jena *et al.*, Elliptical Bloch skyrmion chiral twins in an antiskyrmion system. Nature Commun. **11**, 1115 (2020).

[S9] P. Vir *et al.*, Tetragonal Superstructure of the Antiskyrmion Hosting Heusler Compound $Mn_{1.4}PtSn$. Chem. Mater. **31**, 5876 (2019).

[S10] P. Vir *et al.*, Anisotropic topological Hall effect with real and momentum space Berry curvature in the antiskrymion-hosting Heusler compound $Mn_{1.4}PtSn$. Phys. Rev. B **99**, 140406 (R) (2019).

[S11] P. Marchand, L. Marmet, Binomial smoothing filter: A way to avoid some pitfalls of least - squares polynomial smoothing. Rev. Sci. Instrum. **54**, 1034 (1983).

[S12] R. Gordon, R. Bender, G. T. Herman, Algebraic Reconstruction Techniques (ART) for three-dimensional electron microscopy and X-ray photography. J. Theor. Biol. **29**, 471 (1970).

[S13] W. Voegeli *et al.*, Multibeam x-ray optical system for high-speed tomography. Optica **7**, 514 (2020)

[S14] L. Peng *et al.*, Controlled transformation of skyrmions and antiskyrmions in a non-centrosymmetric magnet. Nature Nanotech. **15**, 181 (2020).

[S15] M. Saito *et al.*, Magnetic Control of Crystal Chirality and the Existence of a Large Magneto-Optical Dichroism Effect in CuB_2O_4. Phys. Rev. Lett. **101**, 117402 (2008).